Advanced coarse-grained model for fast simulation of nascent polypeptide chain dynamics within the ribosome

Shiqi Yu[1], Artem Kushner[2], Ella Teasell[2], Wenjun Zhao[2], Simcha Srebnik[1*] and Khanh Dao Duc[2*]

[1]Department of Chemical and Biological Enginnering, University of British Columbia, Vancouver, BC V6T 1Z3, Canada
[2]Department of Mathematics, University of British Columbia, Vancouver, BC V6T 1Z4, Canada

*Equal contribution
†To whom correspondence should be addressed: ssrebnik@mail.ubc.ca, khanh.daoduc@ubc.ca

Abstract

The nascent polypeptide exit tunnel (NPET) is a sub-compartment of the ribosome that constrains the dynamics of nascent polypeptide chains during protein translation. Simulating these dynamics has been limited due by the spatial scale of the ribosome and the temporal scale of elongation. Here, we present an automated pipeline to extract the geometry of the NPET and the ribosome surface at high resolution from any ribosome structure. We further convert this into a coarse-grained (CG) bead model that can be used in molecular simulations. This CG model more accurately captures NPET geometry than previous representations and allows for the simulation of co- and post-translational processes that are computationally prohibitive with all-atom approaches. In particular, we illustrate how the CG model may be used to simulate the elongation dynamics of the nascent polypeptide and its escape post-translation, as well as evaluate free energy landscapes and electrostatic interactions.

Introduction

The ribosome is a large RNA-protein complex that mediates protein synthesis from messenger RNA (mRNA) during translation. This process requires the formation of a peptide bond at the peptidyl-transferase center (PTC), which is deeply embedded within the large ribosomal subunit [1]. As peptides get added, the nascent polypeptide chain passes through the nascent polypeptide exit tunnel (NPET). The NPET is a narrow conduit, approximately 100 Å length, that connects the PTC to the ribosome's solvent-exposed surface [2]. Over the past decades, experimental efforts have focused on quantifying interactions between the nascent chain and ribosome and elucidating their impact on protein folding and translation arrest [3–6] to understand how NPET dynamically influences protein synthesis [7, 8]. Given the tunnel's dimensions and the complexity of these interactions, molecular dynamics simulations have emerged as both a complement and alternative to experimental methods, providing atomic-level insights into nascent chain interactions at the NPET [9–12].

Simulations involving internal and external features of ribosomes are challenging due to the sheer size a complexity of the ribosome. Bacterial and eukaryotic ribosomes measuring about 20 nm and 30 nm, respectively [13,14]. As such, running even a 10-nanosecond ribosome simulation on a single GPU may take a full day, and microsecond-scale simulations may extend over several months [9]. Whole-ribosome simulations therefore remain exceedingly rare [15] and most molecular dynamics (MD) studies focus exclusively on the tunnel region [16–21]. Yet, even these reduced models comprise tens of thousands of atoms [21] and create a substantial computational burden. Several other

studies employ cylindrical approximations with varying radii to model the exit tunnel and examine protein escape dynamics [22–24]. However, such studies risk oversimplifying some potentially important geometric features of the NPET [25]. Moreover, most models fail to consider the ribosome's solvent-exposed surface, which is known to modulate folding and translation dynamics of the nascent polypeptides as they emerge from the NPET [4, 26, 27]. Notably, intermolecular interactions between the ribosome and specific amino acid (aa) residues at the N-terminus are known to perturb co-translation folding [28] and regulate translation fidelity [29] of nascent chains, and hence should not be neglected in models aiming to capture the ribosome's role in modulating translation dynamics.

All-atom MD simulations have historically been limited to treating one or few species due to their computational expense. However, the recent surge in high-resolution ribosome structures obtained through cryo-electron microscopy [30] has revealed unprecedented heterogeneity across species and domains of life [31]. Comparative studies have demonstrated how some important structural variations in the NPET of bacteria and eukaryotes significantly impact nascent chain dynamics [20, 25]. This structural diversity amplifies the need of alleviating computational costs and facilitating efficient modeling of the NPET environment. This expanding structural dataset can be leveraged to comprehensively explore the functional role of the NPET across evolutionary lineages.

To address these computational limitations, we developed a pipeline to construct coarse-grained (CG) models of NPET and ribosome surface from any given ribosome structure that enables rapid simulations of nascent polypeptide chain dynamics. When utilized with coarse-grained models of proteins [32], the model allows for simulating dynamics at the time scale of protein translation. Our approach converts empty space voxels from the ribosome 3D structure into a 3D mesh of the NPET, that is subsequently used to create an efficient CG model for studying translation-related processes. We benchmark our model against established tunnel representations, evaluating its geometric accuracy and computational efficiency in simulating nascent polypeptide dynamics. We then demonstrate the versatility of the model through various applications, including simulating co-translational and post-translational processes, as well as comparison of energy profiles, and extension to modeling electrostatic potential, showing its potential as a tool for future investigations of nascent polypeptide chain interactions and dynamics across diverse ribosome structures.

Methods

Modeling the NPET interior and ribosome exterior surfaces

To build a CG model of the NPET and ribosome, we first extract the surface of the ribosome and the interior surface of the NPET as regular meshes. For any arbitrary atomic model of the ribosome (obtained from the PDB or other database [30] as a `.cif` file), we run the following protocols:

Exterior ribosome surface

We parse [33] the ribosome `.cif` file to extract 3D coordinates of atoms, which are cast to a pointcloud. A pointset that represents only the surface atoms is extracted via Delaunay triangulation [34] from this initial pointcloud. Orientation vectors known as normals are estimated [35] on this surface pointset to establish what constitutes the interior and exterior relative to the surface pointset. Poisson surface reconstruction [36] is applied to the normal-estimated pointset which yields a smooth mesh of the ribosome surface.

Interior NPET surface

1. The locations of the PTC and the constriction site are retrieved from the API of the `riboxyz` project: `api.ribosome.xyz` (for a precise definition of how their coordinates are calculated, see SI file)

2. The pointcloud of the given ribosome structure is obtained by collecting its atoms' positions from the corresponding `.mmcif` record from the PDB. Any fragments that might be occupying the tunnel (*e.g.* nascent peptide chains and ligands) are removed as needed.

3. Using the PTC and the constriction site coordinates as the main axis, we construct a cylindrical mask with radius of 35 Å and height of 120 Å with the PTC at the base.

4. Atoms contained in the mask are projected onto a binary voxel grid of the same dimensions as the cylindrical mask. Atom positions activate (with value set to 1) voxels whose centers fall within a sphere of radius 2 Å from them. The grid is clipped with the surface of the whole ribosome (produced above) to discard the empty space past the tunnel exit port (optional if the surface is not modeled).

5. Zero-voxels correspond to the NPET interior space and inter-polymeric space pockets. We use DBSCAN [37] density-based clustering algorithm to distinguish the central and biggest cluster corresponding to the NPET from the other pockets. We run DBSCAN two times, first on the entire grid (with default parameters $\varepsilon = 5.5$ and $min_samples = 600$) to detect major clusters, and second on the central cluster ($\varepsilon = 3$ and $min_samples = 120$) to sharpen the cluster revealing atomic-scale features.

6. Normals on the final cluster's points are corrected to point outwards with respect to the tunnel interior. Poisson Surface reconstruction [36] is applied to the pointset to produce a mesh.

Coarse-grained representation of the ribosome tunnel and surface

The aforementioned mesh structure serves as the initial scaffold for the CG model, with CG beads placed at the centroid of the triangular mesh. The beads representing the NPET are placed along the surface normal at a distance corresponding to the radius of the bead to properly capture the cavity. For the ribosome surface, the CG beads are placed directly on the mesh. If necessary, additional CG beads can be added or removed on the mesh vertices or edges. The centroids and normal vectors of the triangle meshes are computed using the PyMeshLab library in Python [38]. LAMMPS "delete_atoms" command [39] is used to delete atoms to ensure an open NPET exit port and reduce the computational costs by deleting overlapping CG beads.

Dynamic simulations of nascent chains

A CG protein model is used for the simulations of nascent chain dynamics. Each residue is modeled by a triplet of beads representing the backbone units, where the central bead of each triplet is designated as either neutral, positively charged, or negatively charged. Lennard-Jones (LJ) potential is used to model the short-range intermolecular interactions between non-bonded residues [40]. Intramolecular interactions are modeled with a harmonic bond potential between neighboring residues. For simplicity, the harmonic angle potential and the dihedral force are neglected. The screened Coulomb potential is used for electrostatic interactions.

To simulate post-translational dynamics within the NPET, CG beads of the nascent chain are initially aligned along the tunnel centerline with the C-terminus positioned at the PTC. The attached polypeptide chain is first equilibrated. The C-terminus is then released. Co-translational dynamics are modeled by simulating the intermittent addition of beads at the PTC at a constant rate. The chain is advanced by a distance equal to half the bond length towards the exit to introduce new beads. During each interval between bead additions, the nascent chain is attached at the PTC. This process is repeated iteratively until the desired chain length is reached. For details on the MD protocol and force field parameters, see SI file.

Mapping effective charges onto the CG beads

The effective potential at the center of each CG bead at the NPET, j, is calculated using the screened potential, ϕ_j, summed over all charged residues (lysine, arginine, glutamate, and aspartate) and nucleic acids within a certain distance (*e.g.*, 50 Å) of the tunnel centerline, as

$$\phi_j = \sum_{i=1}^{n} \frac{q_i}{4\pi\,\varepsilon_0\,\varepsilon_r} \frac{e^{-\kappa\, r_{ij}}}{r_{ij}} \tag{1}$$

where r_{ij} is the distance between the charged atom, i, and the CG bead, j. q_i is the atom charge, ε_0 is the vacuum permittivity, ε_r is the dielectric constant, and κ is the inverse Debye length. The coordinates of the charged residues are extracted using PyMOL and, for simplicity, assigned to their respective C_α atoms [41]. The positions of negatively charged rRNA atoms are placed on the backbone phosphorus atoms. The value of κ is taken to be 0.14 Å^{-1}. The dielectric constant, ε_r, can be set to unity for explicit solvent simulations, can be used to best fit the experimental data [3], or can be estimated in the range of 4 to 80 [42]. The effective charge of each CG bead of NPET is then evaluated from $q_{j,eff} \propto \phi_j R$, where R is the bead radius, set as 1.8 Å [43]. The proportionality constant is chosen to align the induced potential along the tunnel centerline of the CG model with that from the atomistic model using least squares optimization.

While the effective charge of each CG bead of the ribosome surface can be similarly calculated as above, we alternatively propose to calculate the effective electrostatic potential for implicit solvent simulations using Adaptive Poisson-Boltzmann Solver (APBS) in PyMOL [44,45]. The calculations of the linearized Poisson–Boltzmann equation (PBE) [45] are performed at 0.15 M ionic strength in monovalent salt, 310K, solute dielectric constant of 4 and a solvent dielectric constant of 80 [46]. The grid spacing is set to 1 Å. All other parameters of the APBS input file are kept at the default settings. The effective potentials at the centers of the CG beads are then obtained through three-dimensional cubic interpolation of the grid-based data from APBS.

Datasets

The structures used to construct the mesh of the NPET and ribosome surface in this paper are high-resolution atomic models of the ribosome from *H.sapiens* and *E.coli*, deposited in the Protein Data Bank (PDB) with codenames 4UG0 and 6WD4 respectively.

Software and implementation

Our pipeline runs in Python, using a combination of packages including `numpy` [47], `pyvista` [34], `scipy` [48], with the code and illustrative notebooks publicly accessible on GitHub. MD simulations were conducted using LAMMPS (released version: 29 Aug 2024) [49] on a single CPU compute node with a consumer-line PC with 1.4 GHz Quad-Core Intel Core i5 and 8GB RAM memory. The

coordinate extractions of the tunnel centerline, charged residues and heavy atoms were performed in PyMOL [50]. Visualizations of the coarse-grained models and nascent chain dynamics are carried out with VMD [51] and OVITO [52]. All downstream analyses were conducted using custom Python scripts.

Results

Coarse grained modeling of the ribosome surface and NPET

We developed a computational pipeline to generate coarse-grained models of the NPET and ribosome surface from any given structure, as shown in Figure 1a and detailed in the Methods section. Beginning with an atomistic model of the ribosome, the exit tunnel is first identified based on landmarks that define the PTC and constriction site. Atoms within a cylindrical volume surrounding the tunnel are used to extract the tunnel surface as a mesh through DBSCAN clustering and Poisson surface reconstruction (Figure 1b). CG beads are then placed on the mesh to form a CG representation of the tunnel surface. The ribosome surface is similarly captured (Figure 1c). The CG assembly, integrating both the tunnel and ribosome surface can be seen in 3D in Supplementary Video S1.

Comparison with other models

The extent to which the CG model more accurately captures the NPET geometry was evaluated by comparing it to the model obtained by running MOLE, a cavity search algorithm [53] that was used in previous recent geometric studies of the NPET [25, 54]. As this algorithm yields a set of spheres lining along a centerline from the PTC to the exit port, it likely fails to capture irregularities along cross sections of the NPET. Taking ribosomes 4UG0 (*H.sapiens*) and 6WD4 (*E.coli*) as examples from different life domains, we used MOLE2.5 [55] to extract the NPET model and compared the volume produced with our method. To do so, we also divided the tunnel into three regions shown in Figure 2a, namely the upper, lower and exit regions. These regions are separated by the constriction site (see Methods), and conserved residues K68 in uL23 (bacteria), or R28 in eL39 (eukaryotes) [25, 56]. As shown in Figure 2b for 4UG0, the CG model encompasses a volume that is significantly larger, with $3.2e4$ ($2.9e4$ for 6WD4, see Figure S1), compared to $7.3e3$ ($9.5e3$ for 6WD4) for the spherical model. While the upper and lower regions in the CG model are 53% and 82% larger (45% and 71% for 6WD4), respectively, we observed that most of the volume discrepancy concentrates in the exit region, where the difference yields an order of magnitude difference, with $1.6e4$ for the CG model compared to $1.5e3$ for the spherical ($1.2e4$ and $2.7e3$ for 6WD4). Overall, the CG model provides a more comprehensive representation of the NPET's internal space, particularly at the exit port and interface with the external surface. A visualization comparing the volumes of the two tunnel models is provided in the Supplementary Video S2.

To evaluate the potential benefit of the CG model in MD simulations, we further quantified the number of heavy atoms (shown in Figure 2c) that is typically required to simulate the NPET environment using an all-atom representation. For 4UG0 we plot the number of atoms that are located within a distance r from the tunnel centerline (defined from the spherical model) in Figure 2d (corresponding results for 6WD4 are shown in Figure S1c and d). The number of atoms required for the model grows super-linearly, with approximately 5000 atoms for $r = 20$ Å, needed to capture all the atoms lining the NPET. Note that to capture the exit port, this number should be higher due to its large radius (Figure 2b). In comparison, our CG model for 4UG0 contains 2500 beads,

that were set with a radius of 1.8 Å to be watertight. When considering an implicit solvent CG protein model like that used in our following simulations, this number can be further reduced to $\sim$ 1600. As a result, this substantial reduction in particle count enhances simulation efficiency, while preserving the structural integrity of the tunnel.

Simulations of nascent chain dynamics

We demonstrate two applications of our CG model for MD simulations. Dynamic trajectory visualizations are provided in Supplementary Videos S3 and S4. For simplicity, the nascent polypeptide is represented using a bead-spring model where each residue comprises a triplet of beads representing backbone units. Detailed parameters are provided in Methods and SI file.

We first simulated the post-translational escape process of a 20-mer polypeptide from the NPET of 4UG0, illustrated in Figure 3a. The escape time of nascent chains can greatly vary within a 1000-fold range [17], with 20-mers exhibiting particularly extended times compared to other chain lengths (see next section for a more detailed explanation). In our example, the simulation completed in approximately 25 minutes, from the equilibrated conformation of the peptide chain with its C-terminus attached to the PTC ($t = 0$), until complete escape ($t = 5e6$ timesteps). A snapshot taken at $t = 4e6$ shows the polypeptide diffusing toward the exit port following PTC release, thus, indicating that the chain remains confined within the upper tunnel region for the majority of the simulation (see next section).

Next, we simulated the co-translational dynamics (elongation) of the polypeptide in the CG model encompassing both the NPET and ribosome surface. To do so, we added each residue to the growing chain at the PTC (see Methods section) at 1e4 time step intervals. Considering a typical elongation rate of $\sim$ 10 codons per second measured in yeast [57], this corresponds to a time step of 10 μs – a timescale characteristic of molecular CG simulations [32]. Figure 3b shows snapshots of the elongation simulations. The 40-mer chain is seen to be contained within the NPET ($t = 1.2e6$), which is consistent with previous findings that ribosomes can accomodate up to 50 residues internally [58, 59]. As elongation progressed to 80 and 100 residues, we see the N-terminal portion interacting with the ribosomal surface before extending into the solvent environment where folding might initiate. The simulation of a 500-mer chain elongation completed in approximately 4 hours, demonstrating that our CG model enables long-timescale protein translation simulations to complete within hours, even on a single CPU core. Table 1 summarizes the simulation timesteps and corresponding CPU runtimes for both post- and co-translational processes, quantifying the computational efficiency of our approach.

Comparison of energy profiles

Focusing on the post-translation escape process illustrated in our first example, we study nascent chain dynamics and the free energy landscape the protein experiences in the NPET. Previously, we employed a simplified cylindrical model [22] to analyze nascent chain free energy profiles within the tunnel. This study revealed that specific chain lengths encounter geometric barriers that impede NPET escape at particular locations. Similarly, we considered here 12-mer and 20-mer polypeptides in the CG tunnel model of 4UG0, and calculated their free energy profiles along the tunnel axis. Free energy (f) landscapes for each polypeptide length were derived from simulations, by summing over the canonical partition function along the tunnel, with $f(r, N, T) = -kT/N \ln \sum e^{-E(r,N)/kT}$ (see [22]), where the sum is over all configuration with C-terminus at position r along the tunnel, k is the Boltzmann constant, N is the number of beads in the polypeptide, and E is the energy of each microstate. Figure 4a compares the energy profiles between the previous simplified cylindrical

geometry and the current CG model. While both approaches reveal two distinct low-energy states, the energy wells in the CG model are notably shallower with lower energy barriers compared to the cylindrical representation. This difference highlights how our accurate CG model provides more nuanced insights into the energetic landscape governing nascent chain transit through the ribosomal tunnel. Moreover, our CG model can presumably capture nuanced differences between tunnels that cannot be captured with simple models.

For the 20-mer polypeptide (Figure 4b), we observed more significant qualitative differences between the two models. The cylindrical model only displayed a single energy well at the constriction site, whereas the CG model revealed a two-potential well profile again, with the deeper well located in the upper tunnel region. We attribute this discrepancy to volume underestimation in the cylindrical model's upper tunnel region (as evidenced in Figure 2b), making it insufficient to accommodate the polymer chain. In contrast, the CG model demonstrates that the upper tunnel region can effectively trap both 12-mer and 20-mer polypeptides—a finding consistent with previous observations that short proteins of these lengths can initiate folding near the PTC [20, 60]. While both models support the general conclusion that tunnel geometry impedes 20-mer polypeptide escape, it is interesting to note that their biophysical interpretations differ for 4UG0, highlighting again the importance of using a more detailed representation of the NPET.

Modeling effective charges

As an RNA-protein complex enriched in charged residues, the ribosome will have significant electrostatic interactions with charged polypeptide chains [17, 61]. To include these interactions in our CG model, we mapped the effective charges for both the ribosome tunnel and surface onto the CG beads. For the beads at the NPET, we used the ribosomal charged residues and nucleic acids within a certain distance of the NPET, and calculated the associated screened potential at each bead (see Eq. (1)), as described in the Methods section. For the ribosome surface, we used the APBS solver in Pymol (see Methods section) to account for the solvent in our calculation of the effective potential. Figure 5a illustrates the charge distribution of the CG model for the 4UG0 ribosome and NPET (see Figure S2a for 6WD4), with both showing predominantly negative charge. Scattered positively charged regions on the ribosome surface are primarily associated with ribosomal proteins [45] as has been observed in cryo-EM ribosome structures.

To evaluate the accuracy of our mapping, we compared the electrostatic potential profiles along the tunnel centerline generated by our CG model with experimental measurement measured at specific positions of the tunnel for an archaeal ribosome [3] (Figure 5b), as well as the electrostatic profile obtained from atomistic simulation of the bacterial ribosome (4V5D) [46] (Figure S2b). The results indicate that the profile from the CG model aligns closely with empirical measurements (see Figure 5b), and shows the same trend as for the atom-based model. We also noted some more significant deviation between the CG and atom-based profiles at the exit port (Figure S2b), that can be attributed to the inclusion of magnesium ions and TIP3P waters in the atom-based model [46].

Discussion

In this paper, we present a pipeline for constructing coarse-grained models of the NPET and ribosome surface for MD simulations of nascent polypeptide chains across various contexts and extended timescales. While traditional methods model the NPET interior using probe-based cavity extraction [62–65], our approach quantizes the volume space into a grid to identify empty voxels. This space-partitioning strategy has recently proven effective for generating highly detailed volumet-

ric mesh representations of biomolecules [66] with a highly parallelizable algorithm that leverages octree data structure. Herein, we leverage KDtree structures due to their available Python implementations for voxel querying.

We also note that while our simulations were conducted on unoptimized CPU environments, substantial computational efficiency improvements can be expected through GPU or accelerator packages [39]. We employed a simplified CG protein model with Lennard-Jones interactions to illustrate the nascent chain dynamics in our CG environment. However, more sophisticated models using established force fields [67] or all-atom representations [68] can explicitly account for side-chain interactions and dynamic behaviors, thereby providing more detailed and accurate representations of translation and folding dynamics.

One significant limitation of our CG model is its inability to capture potentially flexible elements of the NPET and ribosome (such as the lateral stalk [69]) or conformational changes occurring during different steps of translation [70, 71]. Interestingly, Kurkcuoglu *et al.* employed elastic network modeling to investigate ribosomal flexibility [72], identifying three distinct tunnel regions with characteristic harmonic motions: the upper region primarily moving parallel to the tunnel axis, the exit region displaying pronounced perpendicular mobility (potentially facilitating nascent peptide chain dispersion), and the constriction site exhibiting rotational motions that may contribute to polypeptide gating mechanisms. Future work could integrate these insights through a hybrid modeling approach where functionally critical flexible regions—particularly at the constriction site—are represented at atomic resolution. This would maintain computational efficiency while incorporating essential ribosomal dynamics, providing a more complete representation of the translation environment and its impact on nascent chain.

Author Contributions

KDD and SS designed the research. AK, SY, ET and WZ implemented the methods. SY carried out all simulations and analyzed the data. SY, AK, KDD and SS wrote the article.

Acknowledgments

This research is supported by NSERC Discovery Grants RGPIN-2020-05348 and RGPIN-2024-04666.

References

[1] Rodnina, M. V., Beringer, M., and Wintermeyer, W. (2007) How ribosomes make peptide bonds. *Trends in biochemical sciences,* **32**(1), 20–26.

[2] Thommen, M., Holtkamp, W., and Rodnina, M. V. (2017) Co-translational protein folding: progress and methods. *Current opinion in structural biology,* **42**, 83–89.

[3] Lu, J., Kobertz, W. R., and Deutsch, C. (2007) Mapping the electrostatic potential within the ribosomal exit tunnel. *Journal of molecular biology,* **371**(5), 1378–1391.

[4] Masse, M. M., Guzman-Luna, V., Varela, A. E., Mahfuza Shapla, U., Hutchinson, R. B., Srivastava, A., Wei, W., Fuchs, A. M., and Cavagnero, S. (2024) Nascent chains derived from a foldable protein sequence interact with specific ribosomal surface sites near the exit tunnel. *Scientific Reports,* **14**(1), 12324.

[5] Wruck, F., Tian, P., Kudva, R., Best, R. B., von Heijne, G., Tans, S. J., and Katranidis, A. (2021) The ribosome modulates folding inside the ribosomal exit tunnel. *Communications biology,* **4**(1), 523.

[6] Bustamante, C., Alexander, L., Maciuba, K., and Kaiser, C. M. (2020) Single-molecule studies of protein folding with optical tweezers. *Annual review of biochemistry,* **89**(1), 443–470.

[7] Wilson, D. N. and Beckmann, R. (2011) The ribosomal tunnel as a functional environment for nascent polypeptide folding and translational stalling. *Current opinion in structural biology,* **21**(2), 274–282.

[8] Berisio, R., Schluenzen, F., Harms, J., Bashan, A., Auerbach, T., Baram, D., and Yonath, A. (2003) Structural insight into the role of the ribosomal tunnel in cellular regulation. *Nature Structural & Molecular Biology,* **10**(5), 366–370.

[9] Bock, L. V., Gabrielli, S., Kolář, M. H., and Grubmüller, H. (2023) Simulation of complex biomolecular systems: the ribosome challenge. *Annual Review of Biophysics,* **52**(1), 361–390.

[10] Huter, P., Arenz, S., Bock, L. V., Graf, M., Frister, J. O., Heuer, A., Peil, L., Starosta, A. L., Wohlgemuth, I., Peske, F., et al. (2017) Structural basis for polyproline-mediated ribosome stalling and rescue by the translation elongation factor EF-P. *Molecular cell,* **68**(3), 515–527.

[11] Zimmer, M. H., Niesen, M. J., and Miller, T. F. (2021) Force transduction creates long-ranged coupling in ribosomes stalled by arrest peptides. *Biophysical Journal,* **120**(12), 2425–2435.

[12] Lind, C. and Åqvist, J. (2016) Principles of start codon recognition in eukaryotic translation initiation. *Nucleic Acids Research,* **44**(17), 8425–8432.

[13] Makarov, G., Makarova, T., Sumbatyan, N., and Bogdanov, A. (2016) Investigation of ribosomes using molecular dynamics simulation methods. *Biochemistry (Moscow),* **81**, 1579–1588.

[14] Bock, L. V., Kolář, M. H., and Grubmüller, H. (2018) Molecular simulations of the ribosome and associated translation factors. *Current opinion in structural biology,* **49**, 27–35.

[15] Dror, R. O., Dirks, R. M., Grossman, J., Xu, H., and Shaw, D. E. (2012) Biomolecular simulation: a computational microscope for molecular biology. *Annual review of biophysics,* **41**(1), 429–452.

[16] Bui, P. T. and Hoang, T. X. (2020) Protein escape at the ribosomal exit tunnel: Effect of the tunnel shape. *The Journal of Chemical Physics,* **153**(4).

[17] Nissley, D. A., Vu, Q. V., Trovato, F., Ahmed, N., Jiang, Y., Li, M. S., and O'Brien, E. P. (2020) Electrostatic interactions govern extreme nascent protein ejection times from ribosomes and can delay ribosome recycling. *Journal of the American Chemical Society,* **142**(13), 6103–6110.

[18] Contreras Martínez, L. M., Martínez-Veracoechea, F. J., Pohkarel, P., Stroock, A. D., Escobedo, F. A., and DeLisa, M. P. (2006) Protein translocation through a tunnel induces changes in folding kinetics: a lattice model study. *Biotechnology and bioengineering,* **94**(1), 105–117.

[19] Kirmizialtin, S., Ganesan, V., and Makarov, D. E. (2004) Translocation of a β-hairpin-forming peptide through a cylindrical tunnel. *The Journal of chemical physics,* **121**(20), 10268–10277.

[20] Chwastyk, M. and Cieplak, M. (2021) Nascent folding of proteins across the three domains of life. *Frontiers in Molecular Biosciences,* **8**, 692230.

[21] Petrone, P. M., Snow, C. D., Lucent, D., and Pande, V. S. (2008) Side-chain recognition and gating in the ribosome exit tunnel. *Proceedings of the National Academy of Sciences,* **105**(43), 16549–16554.

[22] Yu, S., Srebnik, S., and Duc, K. D. (2023) Geometric differences in the ribosome exit tunnel impact the escape of small nascent proteins. *Biophysical Journal,* **122**(1), 20–29.

[23] Bui, P. T. and Hoang, T. X. (2018) Protein escape at the ribosomal exit tunnel: Effects of native interactions, tunnel length, and macromolecular crowding. *The Journal of Chemical Physics,* **149**(4).

[24] Bui, P. T. and Hoang, T. X. (2016) Folding and escape of nascent proteins at ribosomal exit tunnel. *The Journal of chemical physics,* **144**(9).

[25] Dao Duc, K., Batra, S. S., Bhattacharya, N., Cate, J. H., and Song, Y. S. (2019) Differences in the path to exit the ribosome across the three domains of life. *Nucleic acids research,* **47**(8), 4198–4210.

[26] Knight, A. M., Culviner, P. H., Kurt-Yilmaz, N., Zou, T., Ozkan, S. B., and Cavagnero, S. (2013) Electrostatic effect of the ribosomal surface on nascent polypeptide dynamics. *ACS chemical biology,* **8**(6), 1195–1204.

[27] Waudby, C. A., Burridge, C., Cabrita, L. D., and Christodoulou, J. (2022) Thermodynamics of co-translational folding and ribosome-nascent chain interactions. *Current Opinion in Structural Biology,* **74**, 102357.

[28] Cassaignau, A. M., Włodarski, T., Chan, S. H., Woodburn, L. F., Bukvin, I. V., Streit, J. O., Cabrita, L. D., Waudby, C. A., and Christodoulou, J. (2021) Interactions between nascent proteins and the ribosome surface inhibit co-translational folding. *Nature Chemistry,* **13**(12), 1214–1220.

[29] Fujii, K., Susanto, T. T., Saurabh, S., and Barna, M. (2018) Decoding the function of expansion segments in ribosomes. *Molecular cell,* **72**(6), 1013–1020.

[30] Kushner, A., Petrov, A. S., and Dao Duc, K. (2023) RiboXYZ: a comprehensive database for visualizing and analyzing ribosome structures. *Nucleic Acids Research,* **51**(D1), D509–D516.

[31] Poitevin, F., Kushner, A., Li, X., and Dao Duc, K. (2020) Structural heterogeneities of the ribosome: new frontiers and opportunities for cryo-EM. *Molecules,* **25**(18), 4262.

[32] Kmiecik, S., Gront, D., Kolinski, M., Wieteska, L., Dawid, A. E., and Kolinski, A. (2016) Coarse-grained protein models and their applications. *Chemical reviews,* **116**(14), 7898–7936.

[33] Cock, P. J., Antao, T., Chang, J. T., Chapman, B. A., Cox, C. J., Dalke, A., Friedberg, I., Hamelryck, T., Kauff, F., Wilczynski, B., et al. (2009) Biopython: freely available Python tools for computational molecular biology and bioinformatics. *Bioinformatics,* **25**(11), 1422.

[34] Sullivan, C. and Kaszynski, A. (2019) PyVista: 3D plotting and mesh analysis through a streamlined interface for the Visualization Toolkit (VTK). *Journal of Open Source Software,* **4**(37), 1450.

[35] Zhou, Q.-Y., Park, J., and Koltun, V. (2018) Open3D: A modern library for 3D data processing. *arXiv preprint arXiv:1801.09847,*.

[36] Kazhdan, M., Bolitho, M., and Hoppe, H. (2006) Poisson surface reconstruction. In *Proceedings of the fourth Eurographics symposium on Geometry processing* Vol. 7, .

[37] Deng, D. (2020) DBSCAN clustering algorithm based on density. In *2020 7th international forum on electrical engineering and automation (IFEEA)* IEEE pp. 949–953.

[38] Muntoni, A. and Cignoni, P. PyMeshLab. (January, 2021).

[39] Thompson, A. P., Aktulga, H. M., Berger, R., Bolintineanu, D. S., Brown, W. M., Crozier, P. S., In't Veld, P. J., Kohlmeyer, A., Moore, S. G., Nguyen, T. D., et al. (2022) LAMMPS-a flexible simulation tool for particle-based materials modeling at the atomic, meso, and continuum scales. *Computer Physics Communications,* **271**, 108171.

[40] Rizuan, A., Jovic, N., Phan, T. M., Kim, Y. C., and Mittal, J. (2022) Developing bonded potentials for a coarse-grained model of intrinsically disordered proteins. *Journal of chemical information and modeling,* **62**(18), 4474–4485.

[41] Bui, P. T. and Hoang, T. X. (2021) Hydrophobic and electrostatic interactions modulate protein escape at the ribosomal exit tunnel. *Biophysical Journal,* **120**(21), 4798–4808.

[42] Joiret, M., Kerff, F., Rapino, F., Close, P., and Geris, L. (2022) Ribosome exit tunnel electrostatics. *Physical Review E,* **105**(1), 014409.

[43] Jorgensen, W. L. and Tirado-Rives, J. (1988) The OPLS force field for proteins. Energy minimizations for crystals of cyclic peptides and crambin. *J. Am. Chem. Soc,* **110**(6), 1657–1666.

[44] Dolinsky, T. J., Nielsen, J. E., McCammon, J. A., and Baker, N. A. (2004) PDB2PQR: an automated pipeline for the setup of Poisson–Boltzmann electrostatics calculations. *Nucleic acids research,* **32**(suppl_2), W665–W667.

[45] Baker, N. A., Sept, D., Joseph, S., Holst, M. J., and McCammon, J. A. (2001) Electrostatics of nanosystems: application to microtubules and the ribosome. *Proceedings of the National Academy of Sciences,* **98**(18), 10037–10041.

[46] Wang, J., Karki, C., Xiao, Y., and Li, L. (2020) Electrostatics of prokaryotic ribosome and its biological implication. *Biophysical Journal,* **118**(5), 1205–1212.

[47] Harris, C. R., Millman, K. J., Van Der Walt, S. J., Gommers, R., Virtanen, P., Cournapeau, D., Wieser, E., Taylor, J., Berg, S., Smith, N. J., et al. (2020) Array programming with NumPy. *Nature,* **585**(7825), 357–362.

[48] Virtanen, P., Gommers, R., Oliphant, T. E., Haberland, M., Reddy, T., Cournapeau, D., Burovski, E., Peterson, P., Weckesser, W., Bright, J., et al. (2020) SciPy 1.0: fundamental algorithms for scientific computing in Python. *Nature methods,* **17**(3), 261–272.

[49] Plimpton, S. (1995) Fast parallel algorithms for short-range molecular dynamics. *Journal of computational physics,* **117**(1), 1–19.

[50] DeLano, W. L. et al. (2002) Pymol: An open-source molecular graphics tool. *CCP4 Newsl. Protein Crystallogr,* **40**(1), 82–92.

[51] Humphrey, W., Dalke, A., and Schulten, K. (1996) VMD: visual molecular dynamics. *Journal of molecular graphics,* **14**(1), 33–38.

[52] Stukowski, A. (2009) Visualization and analysis of atomistic simulation data with OVITO–the Open Visualization Tool. *Modelling and simulation in materials science and engineering,* **18**(1), 015012.

[53] Berka, K., Sehnal, D., Bazgier, V., Pravda, L., Svobodova-Varekova, R., Otyepka, M., and Koca, J. (2017) Mole 2.5-Tool for Detection and Analysis of Macromolecular Pores and Channels. *Biophysical Journal,* **112**(3), 292a–293a.

[54] Yasuda, T., Morita, R., Shigeta, Y., and Harada, R. (2024) Ribosome Tunnel Environment Drives the Formation of α-Helix during Cotranslational Folding. *Journal of Chemical Information and Modeling,* **64**(16), 6610–6622.

[55] Sehnal, D., Bittrich, S., Deshpande, M., Svobodová, R., Berka, K., Bazgier, V., Velankar, S., Burley, S. K., Koča, J., and Rose, A. S. (2021) Mol* Viewer: modern web app for 3D visualization and analysis of large biomolecular structures. *Nucleic acids research,* **49**(W1), W431–W437.

[56] Kolář, M. H., McGrath, H., Nepomuceno, F. C., and Černeková, M. (2024) Three stages of nascent protein translocation through the ribosome exit tunnel. *Wiley Interdisciplinary Reviews: RNA,* **15**(6), e1873.

[57] Ingolia, N. T., Lareau, L. F., and Weissman, J. S. (2011) Ribosome profiling of mouse embryonic stem cells reveals the complexity and dynamics of mammalian proteomes. *Cell,* **147**(4), 789–802.

[58] Nilsson, O. B., Hedman, R., Marino, J., Wickles, S., Bischoff, L., Johansson, M., Müller-Lucks, A., Trovato, F., Puglisi, J. D., O'Brien, E. P., et al. (2015) Cotranslational protein folding inside the ribosome exit tunnel. *Cell reports,* **12**(10), 1533–1540.

[59] Kolář, M. H., Nagy, G., Kunkel, J., Vaiana, S. M., Bock, L. V., and Grubmüller, H. (2022) Folding of VemP into translation-arresting secondary structure is driven by the ribosome exit tunnel. *Nucleic acids research,* **50**(4), 2258–2269.

[60] Neidigh, J. W., Fesinmeyer, R. M., and Andersen, N. H. (2002) Designing a 20-residue protein. *Nature structural biology,* **9**(6), 425–430.

[61] Dao Duc, K. and Song, Y. S. (2018) The impact of ribosomal interference, codon usage, and exit tunnel interactions on translation elongation rate variation. *PLoS genetics,* **14**(1), e1007166.

[62] Chovancova, E., Pavelka, A., Benes, P., Strnad, O., Brezovsky, J., Kozlikova, B., Gora, A., Sustr, V., Klvana, M., Medek, P., et al. (2012) CAVER 3.0: a tool for the analysis of transport pathways in dynamic protein structures.

[63] Ho, B. K. and Gruswitz, F. (2008) HOLLOW: generating accurate representations of channel and interior surfaces in molecular structures. *BMC structural biology,* **8**, 1–6.

[64] Sehnal, D., Svobodová Vařeková, R., Berka, K., Pravda, L., Navrátilová, V., Banáš, P., Ionescu, C.-M., Otyepka, M., and Koča, J. (2013) MOLE 2.0: advanced approach for analysis of biomacromolecular channels. *Journal of cheminformatics,* **5**, 1–13.

[65] Maglic, J. B. and Lavendomme, R. (2022) MoloVol: an easy-to-use program for analyzing cavities, volumes and surface areas of chemical structures. *Applied Crystallography,* **55**(4), 1033–1044.

[66] López, J., Botello, S., Herrera, R., and Carrillo-Tripp, M. (2019) Parallel high-performance computing algorithm to generate FEM-compliant volumetric mesh representations of biomolecules at atomic scale. In *Supercomputing: 10th International Conference on Supercomputing in Mexico, ISUM 2019, Monterrey, Mexico, March 25–29, 2019, Revised Selected Papers 10* Springer pp. 318–333.

[67] Monticelli, L., Kandasamy, S. K., Periole, X., Larson, R. G., Tieleman, D. P., and Marrink, S.-J. (2008) The MARTINI coarse-grained force field: extension to proteins. *Journal of chemical theory and computation,* **4**(5), 819–834.

[68] Fischer, A.-L. M., Tichy, A., Kokot, J., Hoerschinger, V. J., Wild, R. F., Riccabona, J. R., Loeffler, J. R., Waibl, F., Quoika, P. K., Gschwandtner, P., et al. (2024) The role of force fields and water models in protein folding and unfolding dynamics. *Journal of Chemical Theory and Computation,* **20**(5), 2321–2333.

[69] Gonzalo, P. and Reboud, J.-P. (2003) The puzzling lateral flexible stalk of the ribosome. *Biology of the Cell,* **95**(3-4), 179–193.

[70] Korostelev, A., Ermolenko, D. N., and Noller, H. F. (2008) Structural dynamics of the ribosome. *Current opinion in chemical biology,* **12**(6), 674–683.

[71] Chowdhury, A. R., Sapkota, D., and Girodat, D. (2024) Conformational changes of ribosomes during translation elongation resolved by molecular dynamics simulations. *Current Opinion in Structural Biology,* **86**, 102804.

[72] Kurkcuoglu, O., Kurkcuoglu, Z., Doruker, P., and Jernigan, R. L. (2009) Collective dynamics of the ribosomal tunnel revealed by elastic network modeling. *Proteins: Structure, Function, and Bioinformatics,* **75**(4), 837–845.

Supplementary Material

Our SI file contains Supplementary methods and figures, and description of the supplementary videos.

TABLES

Table 1: Simulation and CPU times for post- and co-translational processes for different lengths of polypeptides in the coarse-grained tunnel and ribosome surface model of 4UG0.

Simulations	**Time step**	**CPU time** [s]
Post-translation (tunnel escape)	$10,000$	2.71
Elongation (50-mer)	$1.6e6$	1,206
Elongation (100-mer)	$3.2e6$	2,282
Elongation (500-mer)	$1.6e7$	$15,040$

FIGURES

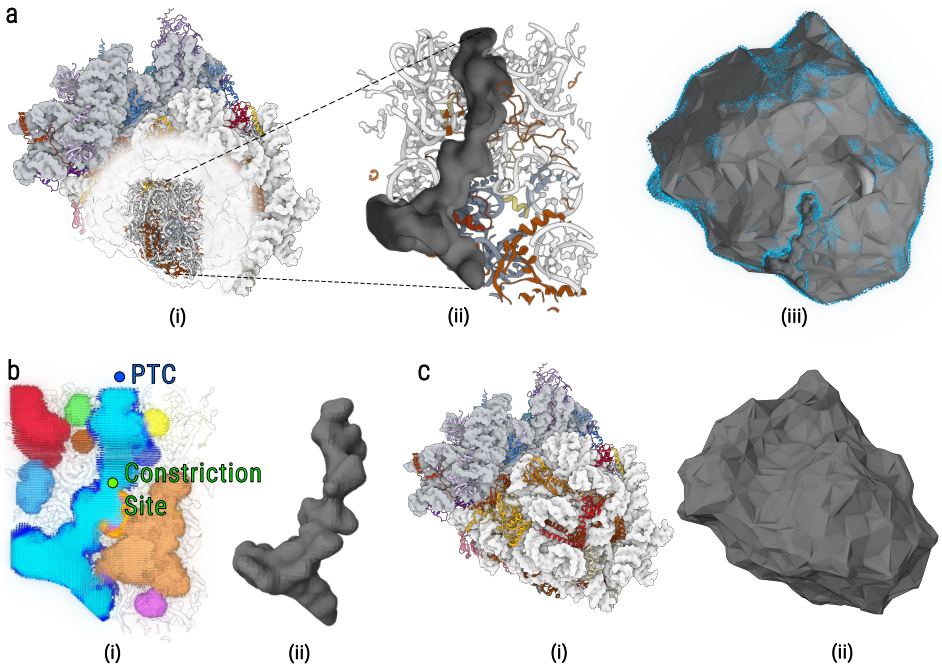

Figure 1: Construction of CG simulation environment illustrated with ribosome structure 4UG0. **(a)** General illustration showing NPET *(ii)* and ribosome surface *(iii)*. Selected representative beads of the CG model are indicated by blue spheres. **(b)** After clustering empty voxels *(i)*, we build the tunnel mesh *(ii)*. **(c)** Mesh produced from the ribosome structure *(i)* using Poisson surface reconstruction *(ii)*.

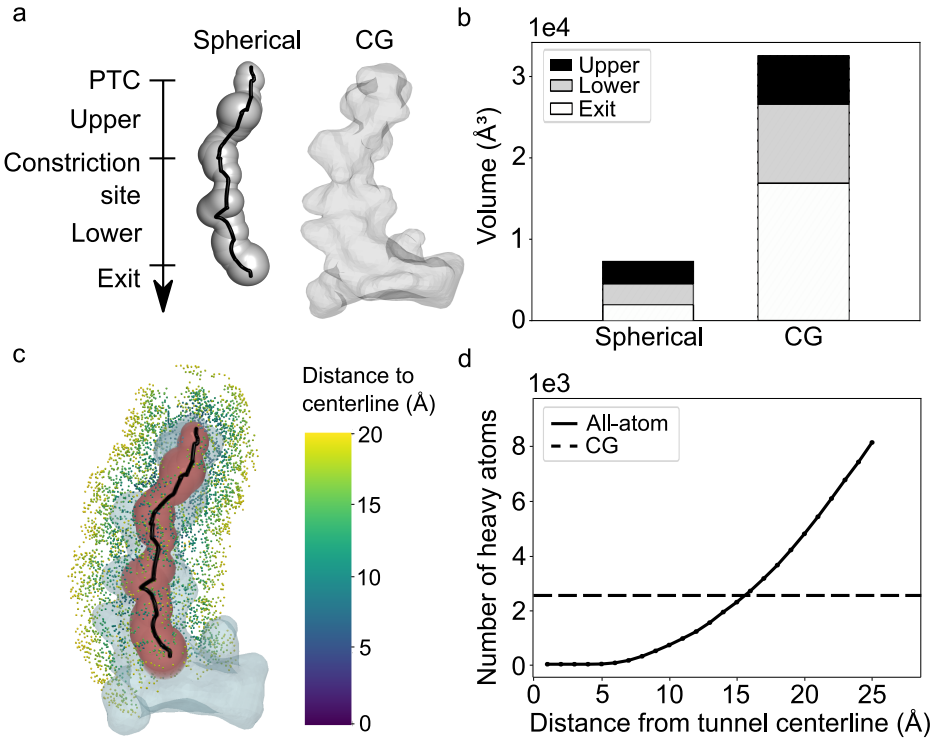

Figure 2: Comparisons of the CG tunnel model with the spherical and all-atom model for 4UG0. **(a)** The MOLE-generated spherical tunnel model (left) and the CG model are represented as a mesh (right). The tunnel is divided into three regions. The upper, lower and exit region are separated by the constriction site and conserved residues in uL23 or eL39. **(b)** Volume of the spherical and CG models in the upper, lower and exit regions. **(c)** An overlay of the CG tunnel model (grey), the spherical model (red) and the tunnel centerline (black). The heavy atoms surrounding the tunnel are colored by distance to the centerline. **(d)** Cumulative number of heavy atoms as a function of distance from the tunnel centerline. The dashed line represents the number of particles in the CG model, approximately 2,500.

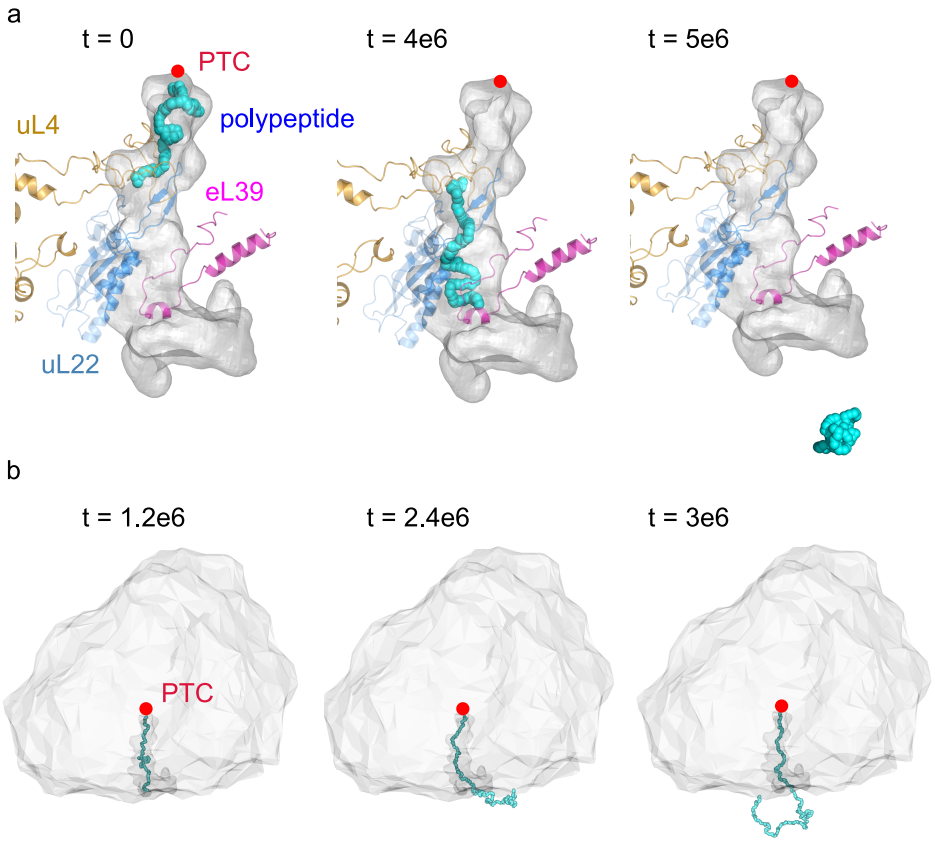

Figure 3: Dynamic simulations of polypeptides within the coarse-grained ribosome exit tunnel model of 4UG0. **(a)** Post-translational dynamics of a 20-mer polypeptide, illustrating its release from the PTC to its full exit from the tunnel (left to right). Ribosomal proteins uL4, uL22, and eL39 are highlighted in orange, blue, and magenta, respectively. These proteins are merely used for visualization purposes, and are not explicitly modeled in the simulations. The PTC is highlighted as a red dot. **(b)** Co-translational process of polypeptide elongating to 40, 80, and 100 amino acid residues. The ribosome surface is modeled to simulate interactions with the protein segment extending beyond the tunnel. Time t represents the simulation time steps.

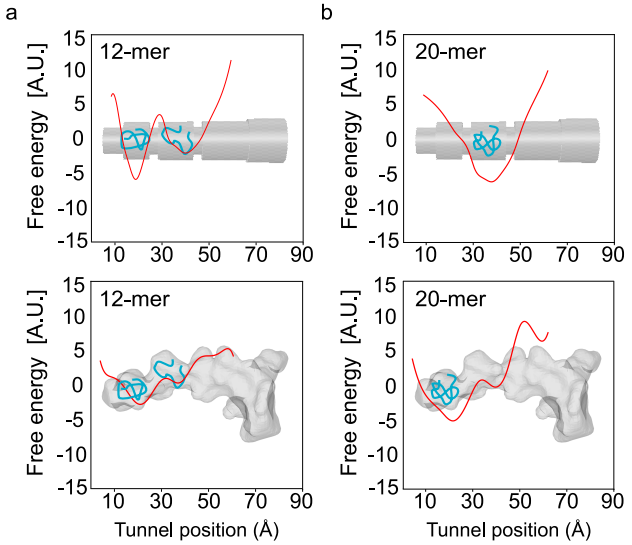

Figure 4: Comparison of free energy landscapes of **(a)** 12-mer and **(b)** 20-mer polypeptide in the cylindrical (upper) [22] and coarse-grained model (lower) of the eukaryotic tunnel 4UG0. The energy was calculated from the sum over the partition function at each position along the tunnel using the C-terminus position. A Savitzky-Golay filter was applied to reduce the noise.

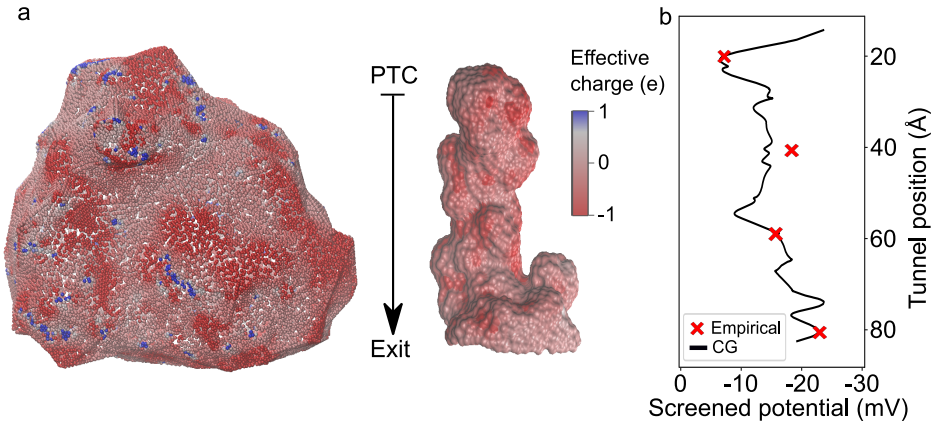

Figure 5: Coarse-grained models of the ribosome surface and tunnel with mapping of effective charges. **(a)** Visualization of effective charges mapped onto the ribosome surface and the exit tunnel of 4UG0. Blue and red beads represent positively and negatively charged beads, respectively. The color scale range was adjusted to improve visualization clarity. **(b)** Electrostatic potential along the tunnel centerline in the archaeal ribosome 1JJ2 derived from the CG model (black curve) compared with experimental data [3] (red crosses).